*Acta of Bioengineering and Biomechanics*
*Vol. 26, No. 3, 2024*

Original paper
DOI: 10.37190/ABB-02469-2024-03

# Kinetic characterization of adolescent scoliosis patients with Lenke 1B+

HUAI WANG, RONGCHANG FU*, KEWEI YANG

Xinjiang University, China.

*Purpose*: The purpose of this study was to investigate dynamic responses of Lenke1B+ spines of adolescent scoliosis patients to different frequencies. *Methods*: Modal analysis, harmonic response analysis and transient dynamics of a full spine model inverted by the finite element method using Abaqus. *Results*: The first-order axial resonance frequency of 4.51 Hz produced a maximum axial displacement of 30.15 mm. Comparison of the five frequencies indicated that the 10 Hz frequency response curve was smoothest, while the amplitude-frequency curve at 4 Hz showed the greatest fluctuations accompanied by resonance phenomena. At the resonance frequency, the maximum axial displacement of the thoracic spine was at T1, being 31.17 mm, while that of the lumbar spine was at L1, with 0.56 mm. The maximum stress of the intervertebral discs was located between T4 and T5, representing 3.496 MPa, the maximum stress in the small joints was located in the concavity between T7 and T8, with 19.97 MPa and the maximum axial displacement was 54.31 mm, located in the convexity between T6 and T7. *Conclusions*: The first-order axial resonance frequency was the most harmful to the patient. The uneven stress distribution in the spine was closely related to the degree of spinal deformity, with the thoracic spine being more sensitive to low frequencies than the lumbar spine. The concave side of the spinal deformity was more prone to stress concentrations while the convex side was more prone to deformity, indicating that disc degeneration and small-joint disease are more likely to occur at the most deformed part of the spine.

*Key words*: *adolescent scoliosis, modal analysis, harmonic response analysis, transient analysis*

## 1. Introduction

Adolescent idiopathic scoliosis (AIS) is a three-dimensional deformity of the spine. The etiology is unknown, and the condition is characterized by imbalance in the coronal, sagittal, and axial positions that occurs in adolescents aged 10–16 years [18]. The prevalence is widely recognized to be 1–4%, and severe scoliosis can bring about physical pain, respiratory damage, lung disease, psychological disorders (autism, depression [29] and even schizophrenia [25]), cosmetic deformities, and reduced quality of life [17], which makes it particularly important to explore the pathological mechanisms underlying AIS.

Epidemiological studies have reported that the probability of pain or injury to the normal spine is increased 1.4–9.5-fold in a vibrating environment [24], and the force aggravates the progression of the deformity curve [30]. To protect scoliosis patients from aggravation in a dynamic loading environment, the kinetic properties of AIS need to be investigated.

Many researchers have investigated the structural characteristics, deformation tendency, and stress distribution of the human spine by the finite element method to explore the mechanism involved in AIS induction [16], [30]. In 2018, Guo and Fan [9] used the L1–S finite element model to determine the effect of changes in disc material properties on the lumbar spine under vertical vibration, while in 2019, Jia et al. [12] analyzed and compared the sinusoidal vibration response of LenkeA, LenkeB and LenkeC lumbar spines under axial loading. Later, in 2021, Zhang et al. [38] performed a static analysis of the lumbar spine of patients with idiopathic scoliosis under six working conditions and, in 2024, Alassaf et al. [1] established a 3D finite element model for T1–L5 static and transient analyses of the lumbar spine under different loads, analyzing the

* Corresponding author: Rongchang Fu, Xinjiang University, China. E-mail: 2781642414@qq.com
Received: June 28th, 2024
Accepted for publication: September 23rd, 2024

stress-strain of the vertebral bones and intervertebral discs. These studies focused on the lumbar spine and did not pay attention to the thoracic spine. However, in the human spine, the thoracic and lumbar spines interact with one another, making it difficult to ignore the characteristics of the whole spine and also to apply conclusions drawn from a study of a specific part of the spine to the spine in general in the clinic. Therefore, in this study, we created a model of the whole spine based on a severe case, and performed a mechanical characterization of the whole spine followed by more localized analysis.

In most current analyses, load is applied using a vertical load at the point of mass or contact surface as this method is a good substitute for physiological compressive loading under *in vivo* conditions when one vertebra is used, but application to the whole spine makes it difficult to maintain stability [4]. The model used in the present study had 12 thoracic vertebrae, 5 lumbar vertebrae, 5 sacral and one caudal vertebra, and the established finite element model is complex, and the commonly used methods cannot support the complex dynamic analysis of this study. In 2007, Renner et al. [28] established an L1–S1 three-dimensional finite element model to test the bending moments in three planes under a large compression follower preload, and concluded that the use of a thermally isotropic truss element to apply compression forces can simulate the follower load path encountered by a normal lumbar spine *in vivo*, and in 2017, Guo and Fan [8] and Shaowei et al. [14] applied the compression follower preload to the lumbar spine three-dimensional finite element model. Several previous studies have taken the optimal path to apply the following loads in the lumbar spine segments, a relatively rare approach in current research on the whole-spine model, and the present study extends this technique of applying load to the whole spine.

In this study, the complexity of the spinal structure was fully considered, and a whole-spine model of patients with AIS with primary thoracic and secondary severe lumbar curvature was established and rigorously validated both statically and dynamically. The following loads were applied to the whole thoracolumbosacral spine by establishing predefined fields and setting temperature coefficients for the thermally isotropic truss elements in Abaqus, after which the self-oscillation frequencies, corresponding vibration shapes and parts of the spine with the greatest deformation were predicted by modal analysis, while the frequency intervals of sensitivity in the whole spine were predicted by frequency response analysis. The most sensitive intervals were analyzed in depth, with investigation at 1.6 s transients within 1.6 under sinusoidal cyclic loading at different frequencies to further explore the effects of cyclic loading at resonant frequencies on the stress–strain of the vertebral body, intervertebral discs, and small joints.

This study helps to explore the underlying biomechanical mechanisms in AIS patients with Lenke1B+, and facilitates the elucidation of the pathology associated with the progression of spinal deformity, intervertebral disc degeneration and arthritis, with a view to providing a theoretical basis and recommendations for the design of clinical treatment programs and the care of patients in their daily lives.

# 2. Materials and methods

## 2.1. Finite element modelling of the thoracolumbosacral spine

The subject of this paper was a 15-year-old female volunteer with severe adolescent idiopathic scoliosis classified as Lenke1B+. The largest Cobb angles measured by the classical method were 42.2° for the thoracic rightward curvature and 21.37° for the lumbar leftward curvature, with lumbar correction type B and thoracic sagittal correction type +.

A single multi-row (64-row) spiral CT was used for scanning the patient plus 3D reconstruction of the spine, using a tomographic thickness of 1.0 mm a pixel size of 0.6953 mm, and a total of 795 images in DCM file format. The threshold value and manual segmentation were set in Mimics to isolate the target region and reconstruct the spine in 3D by repeated erasing, filling and smoothing to obtain a rough model of 640.77 mm. Freeform was used for repeated carving and smoothing, creating small joints between the vertebrae and intervertebral discs to further improve the model, while in Geomagic, the peg was deleted, the surface pieces were constructed, and the surface smoothing was optimized. The mesh delineation and material property settings in HyperMesh were used to generate a 3D finite element model with 446 440 nodes and 224 0713 cells, with cell property settings in Abaqus. The 525.44 mm full-spine model is shown in Fig. 1.

The model consisted of vertebral cortical bone, vertebral cancellous bone, posterior structures, endplates, nucleus pulposus, annulus fibrosus matrix, seven related ligaments, and small joints. There were two types of bone tissue, namely, cortical and cancellous bone, and many ligaments, including the ligamentum flavum and the longitudinal, posterior longitudinal, supraspinous, interspinous, intertransverse interlaminar, and intraar-

ticular capsule ligaments. In this study, 12 thoracic vertebrae, 5 lumbar vertebrae and 9 spinal columns were healed into the sacrum and coccyx, and the layer thickness of vertebral cortical bone was 1 mm [13]. The material properties of the components of the model are shown in Table 1.

Fig. 1. The research model

*Static validation*

To ensure the validity of the thoracic vertebral segments, the simulation method of Jia et al. [13] was used together with the *in vitro* experimental method described by Watkins et al. [32], fully restraining the last thoracic vertebral body and applying 2 Nm of pure moment of lateral bending, 2 Nm of pure moment of flexion, 5 Nm of axial rotation and 50 N of preload to the upper surface of the first thoracic vertebral body in three separate time points, followed by measurement of bending of the left and right sides, anterior and posterior bending, and left and right rotation of the thoracic vertebral body as well as the moment and axial rotation with 50 N preload. The calculations were performed at three time points, measuring the thoracic spine mobility for left and right lateral bending, anterior and posterior bending, and left and right rotation, and compared the data with the experimental data of Watkins et al. [32] and the simulation results of Jia, as shown in the first section in Fig. 3. To ensure the validity of the lumbosacral spine segments under following load, the study referred to the

Table 1. Material properties of the spinal components

| Spinal components | Young's modulus [MPa] | Poisson's ratio | Cross-sectional area [mm$^2$]) | Element type | Density [$10^{-9}$ t/mm$^3$] | References |
|---|---|---|---|---|---|---|
| Cortical bone | 12000 | 0.3 | | S3 | 1.7 | [26] |
| Cancellous bone | 100 | 0.2 | | C3D4 | 1.1 | [5] |
| Posterior structure | 3500 | 0.25 | | C3D4 | 1.4 | [5], [9], [20] |
| Endplate | 500 | 0.25 | | S3 | 1.2 | [20] |
| Nucleus pulpous | 1 | 0.49 | | C3D8 | 1.02 | [20] |
| Annulus substance | 4.2 | 0.45 | | C3D8 | 1.05 | [16], [19] |
| ALL | 7.8 | | 63.7 | T3D2 | 1 | [5], [9], [20] |
| PLL | 10 | | 20 | T3D2 | 1 | [5], [9], [20] |
| LF | 15 | | 40 | T3D2 | 1 | [5], [9], [20] |
| SSL | 8 | | 30 | T3D2 | 1 | [5], [9], [20] |
| ISL | 10 | | 40 | T3D2 | 1 | [5], [9], [20] |
| ITL | 10 | | 3.6 | T3D2 | 1 | [20] |
| CL | 7.5 | | 30 | T3D2 | 1 | [5], [9], [20] |
| Articular capsule | 10 | 0.3 | | C3D4 | 1 | [21] |

## 2.2. Model validation

Under the same load amplitude, dynamic loading can result in more serious potential damage than static loading, so validation of the dynamic characteristics is very necessary [10]. The study used a segmented verification approach for static modal and transient dynamic verification.

*in vitro* experimental method of Renner et al. [28] and the simulation method of Guo et al. [8], and validated five groups of segments, L1–L2, L2–L3, L3–L4, L4–L5 and L5–S1, by segmentation. First, 1200 N of pure following load was applied and the amount of compression was measured, after which 800 N was applied to the five groups of segments, followed by 500 N. Then 800 N following load with 8/–6 Nm forward/backward bending moment was applied to the five sets of segments to

measure their mobility, and these 10 sets of data were compared with the experimental data and the reference data, as shown in the second and third sections of Fig. 3.

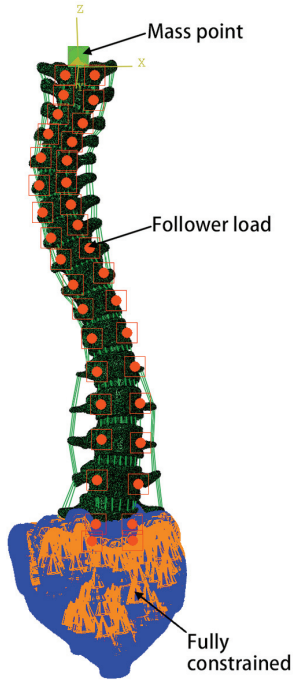


Fig. 2. Application of follower load to the developed thoracolumbosacral vertebral model and the boundary conditions of the model

nusoidal displacement load with a frequency of 1 Hz and an amplitude of 0.6 mm was applied to the center of the intervertebral disc [6]; the anterior–posterior (A–P) force in terms of time is shown in the Figure.

## 2.3. Loads and boundary conditions

In this study, using the established finite element model of the human thoracolumbosacral spine, the effect of the upper body mass on the dynamic characteristics of the model was considered, and a preloaded mass point of 10.5 kg was added 10 mm in front of the center of the upper surface of the most apical vertebrae [9]. Since vertical loading at compressive loads higher than 100 N may lead to collapse of the intact lumbar segments, resulting in difficulty in maintaining stability in the T1–S model, a following load F was used in this study, and to simulate the physiological compression of muscle contraction in the human body, as well as that of gravity on the model used in the present study in the human vertical posture, a following load of 105 N [22] was applied to the finite element model using the optimal path [3]. In this study, the thermal isotropic truss element was set up using Hypermesh software, after which a temperature-predefined field was set up for this

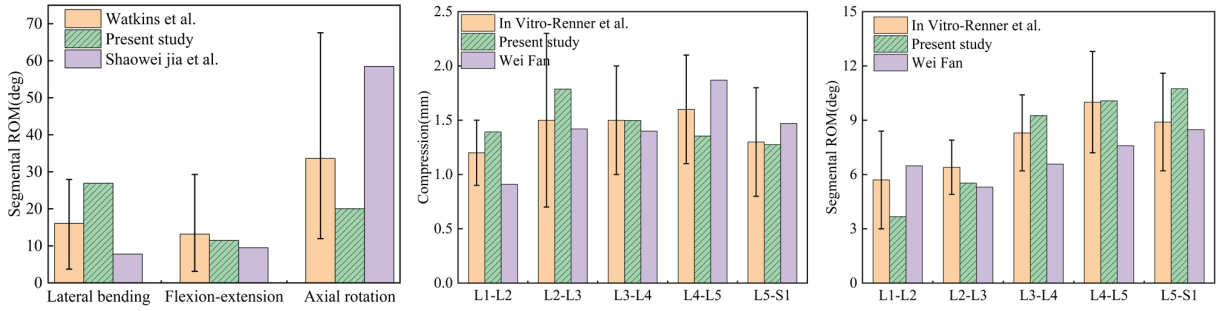


Fig. 3. Comparison between the current predictions and previously published experimental and numerical data

*Modal validation*

The first-order axial modal verification used the simulation data of one, two, and multiple segments disassembled by the study model to compare and validate against published experimental data and finite element simulation data, which were then incorporated into a Table.

*Transient dynamic verification*

With reference to the experiments of Stokes and Gardner-Morse [31], a compressive preload of 642 ± 132 N was applied to the vertebral body to generate an approximate stress of 0.4 MPa in the intervertebral disc, and a si-

element by Abaqus software, so that the compression force was applied on top of each vertebrae by decreasing the temperature of the element unit corresponding to each vertebrae, which resulted in contraction tension. The material properties set in Hypermesh and the parameters set in Abaqus software are shown in Table 2. To simulate the actual situation of human body, six degrees of freedom of the lower surface of the sacrum need to be constrained in the analysis, as shown in Fig. 2.

To understand the structural intrinsic vibration characteristics of the model used in this study, the modal analysis of the finite element model of the thora-

columbosacral spine was conducted using the Lanczos method and extracting the frequency range of 0–30 Hz [13].

Based on the harmonic response analysis of modal analysis, to simulate a realistic dynamic loading environment, damping was considered, and here an equivalent damping ratio of 0.08 obtained from experimental tests was used [11], with a sinusoidal load excitation of ±40 N added to the upper surface of T1 to simulate the dynamic loading environment of a patient with scoliosis in the axial direction, and the frequency range of excitation was set to 0–30 Hz [13].

Based on the transient analysis of the modal superposition method, a sinusoidal axial load of 40 N was applied to the upper surface of the T1 vertebrae using an equivalent damping ratio of 0.08 [13]. Since the common vibration frequencies of vehicles are 3.0–6.0 Hz [35] and the vibration of the vertical direction of the human upper body has strong energy transferability around 4–10 Hz [34], the transients at 3, 4, 5, 6 and 10 Hz were analyzed and compared to explore the transient characteristics of the 1.6 s at different frequencies.

Table 2. Material properties of the temperature truss elements used to apply the follower load

| Young's modulus | Poisson's ratio | Average coefficient of thermal expansion $\alpha$ |
|---|---|---|
| $3.5e^{-6}$ [MPa] | 0.3 | $1.0e^{6}$ [1/°C] |
| Initial temperature $\theta_0$ | final temperature $\theta$ | Cross-sectional area $S$ |
| 0 [°C] | –15 [°C] | 1 [$mm^2$] |

The followed load ($F_t$) in each thermo-isotropic truss element is given by $F_t = Es\alpha\ (\theta_0 - \theta)$.

# 3.Results

## 3.1. Results of model validation

### 3.1.1. Statics verification results

In Figure 3, it can be seen that the data calculated by the model of this study under the corresponding spinal segments and boundary loads were within the error range of the *in vitro* experiments and similar to those of the references, which indicates that the static validation of the model of this study was reasonable and effective, and the results of static analyses carried out with this model were reliable.

### 3.1.2. Kinetic verification results

#### 3.1.2.1. Modal verification results

The first-order axial modal validation is shown in Table 3, showing that the first-order axial modal frequency of the model was between that of the experimental data and the reference data, indicating the reliability of the subsequent modal analysis results.

Table 3. First-order axial resonance frequencies of different segments

| Number of segments | Compressed preload [N]) | Frequency [Hz]) | Data source |
|---|---|---|---|
| One | | | |
| L2–L3 | 0 | 23.6 | [15] |
| L2–L3 | 0 | 22.09 | [4] |
| L2–L3 | 0 | 21.834 | The present study |
| Two | | | |
| L3–L5 | 0 | 18.0 | [16] |
| L3–L5 | 0 | 15.72 | [4] |
| L3–L5 | 0 | 16.535 | The present study |
| L4–S1 | 400 | 17.5 | [7] |
| L4–S1 | 400 | 16.84 | [4] |
| L4–S1 | 400 | 16.669 | The present study |
| Multiple | | | |
| L1–L5 | 0 | 12.2 | [16] |
| L1–L5 | 0 | 10.52 | [4] |
| L1–L5 | 0 | 11.425 | The present study |
| L1–S1 | 400 | 7.77 | [6] |
| L1–S1 | 400 | 9.641 | The present study |

#### 3.1.2.2. Transient dynamic verification results

In Figure 4, it can be seen that the change rule of the model's response curve was consistent with the results of the *in vitro* experiments, and the time of peak appearance was also consistent, indicating that the results of the subsequent steady-state and transient analyses were credible.

In summary, both static and dynamic validation of the model in this study were passed and the results of the dynamic simulation carried out based on the model can be considered informative.

## 3.2. Modal analysis results

The modal analysis of the T1–S finite element model was carried out and the first 6 orders of the intrinsic frequency were extracted, as shown in Table 4, with the displacement change state of its corresponding vibration mode shown in Fig. 5.

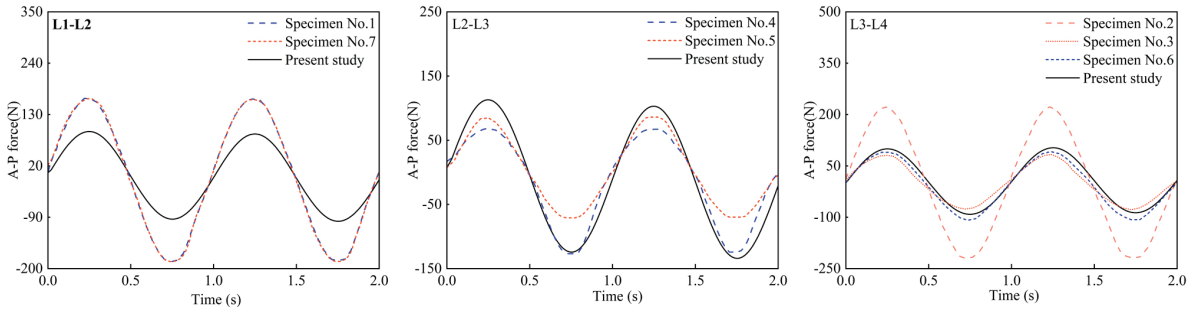


Fig. 4. Comparison of the results of the time-domain response of the present model with the experimental data of Stokes and Gardner-Morse

Table 4. Resonant frequencies and description of vibration

| Orders | Frequency [Hz] | Description of vibration |
|---|---|---|
| 1 | 0.39298 | Overall left and right direction side bending vibration pattern |
| 2 | 0.76770 | Overall front-to-back bending pattern |
| 3 | 4.5145 | Overall twisting around the vertical axis and bending to the right |
| 4 | 14.075 | Overall twisting around the vertical axis and bending to the left |
| 5 | 18.017 | Integral twisting around the vertical axis and bending to the front |
| 6 | 30.046 | Integral twisting around the vertical axis and bending to the front |

In Figure 5, the initial state of the spine is transparent, and the state of the spine after the vibration response is an opaque solid. Axial displacement at the spinal deformity is the most hazardous to the patient, and the largest part of the third-order mode thoracic spine bending can be visualized in red from the vibration pattern diagram, leading to the conclusion that frequencies near 4.5145 Hz are the most hazardous.

## 3.3. Harmonic response analysis results

To further analyze the dynamic response characteristics of the present model under axial cyclic load-

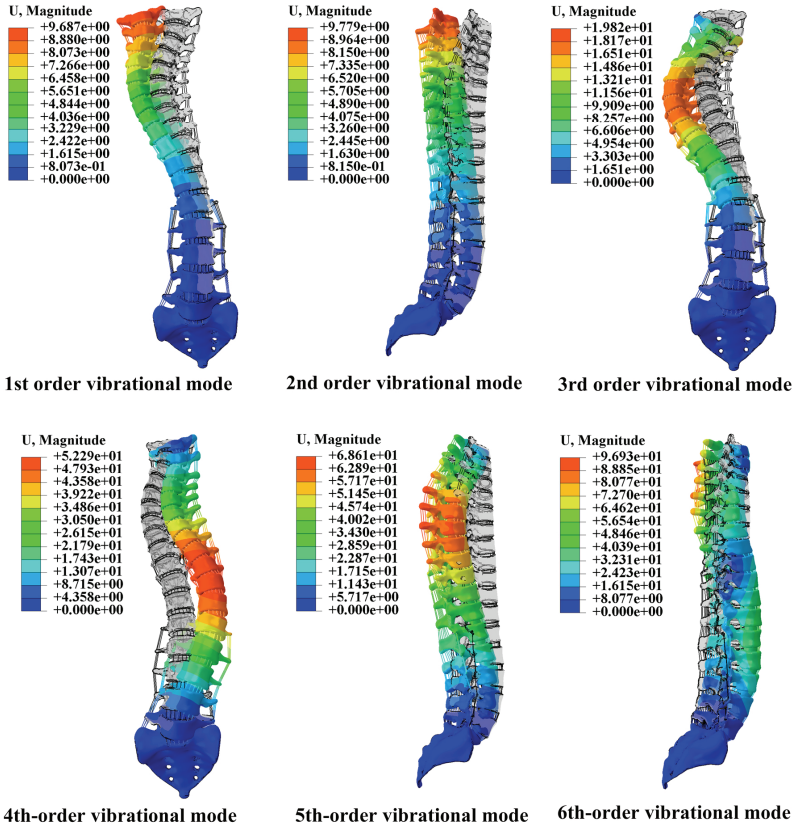


Fig. 5. First six orders of vibration. The contour for the original location of the model is also shown

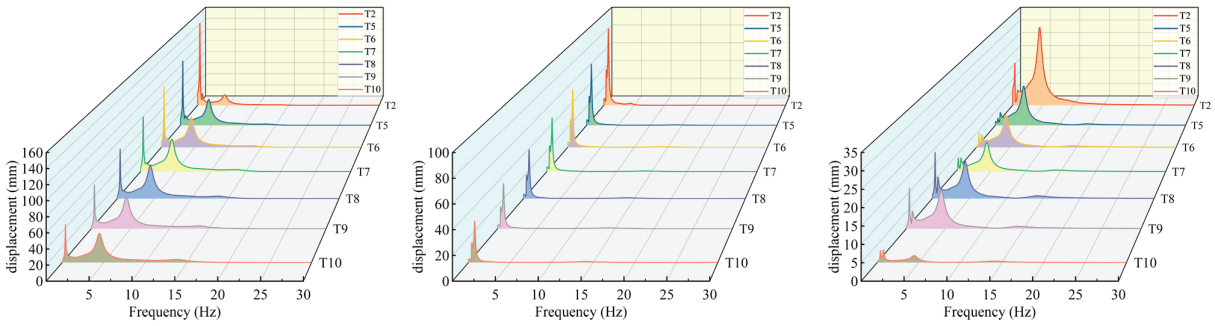


Fig. 6. Amplitude-frequency response of representative vertebrae in coronal, sagittal, and transverse planes

ing, T2 of the parietal vertebrae at the maximum Cobb's angle of the spine and the segments with significant displacement of the third-order modes (T5–T10) were analyzed. According to the anatomical characteristics of the spine, representative nodes were selected at the lateral sides of the pedicles of the vertebral bodies to characterize the variation of vibration amplitude with frequency of the vertebral bodies in the three directions (coronal, sagittal, and transverse planes) as shown in Fig. 6.

From the figure, it can be seen that the representative nodes on each vertebra have obvious vibration peaks near 0.5 and 5 Hz, the frequency of the vibration peaks is consistent with the intrinsic frequency obtained from the modal analysis of each order, and the low-frequency ranges of 0–1 Hz and 4–6 Hz are the sensitive frequency ranges of this model.

## 3.4. Transient dynamics analysis

Because the factor of muscle contraction is considered here, in the results, the axial resonance frequency was significantly reduced from 4.5145 Hz→4.0761 Hz, thus the data of the axial displacements of each vertebral body at the resonance frequency were analyzed based on the difference between the geometrical models of the thoracic vertebral body and the lumbar vertebral body, so that the thoracic vertebral body and the lumbar vertebral body were analyzed independently. The results of the analysis of the mechanical properties of the vertebrae are shown in Fig. 7, where the curves show the characteristics of periodic fluctuation with time.

In the thoracic spine, the axial displacement increased sequentially from T12 to T1. The maximum axial displacement was 31.17 mm. In the lumbar spine, the curve L2 showed the greatest fluctuation, with a maximum axial displacement of 0.56 mm. It is thus clear that the amplitude of the frequency response was greater in the thoracic spine than in the lumbar spine.

In Figure 7, it can be seen that under cyclic loading, the transient characteristics of the 12 spinal segments T1–T12 are similar, with little fluctuation in the lumbar spine response; thus, the T6 vertebrae and the T4–T5 intervertebral discs were used as examples for comparative analyses of the response characteristics of the different loads with the vertebral body (the center of the apex surface as the reference point for the analysis of the data [6]) centered on the axial displacement, and the bulging of the intervertebral discs. The intravertebral disc pressure, von Mises stress in the matrix, and nucleus pulposus pressure were plotted as time curves, as shown in Fig. 8.

The curve shows the characteristics of cyclic fluctuation of the cycle, showing the dynamic load cyclic characteristics and frequency dependence, with the fluctuation of the largest curve frequency being 4 Hz. It is possible that this frequency is closest to the resonance frequency so the emergence of the response is the most drastic.

Compared to other frequencies, the fluctuation of the curve at the high frequency of 10 Hz frequency was the most flat, and the fluctuation of the dynamic response curve at the low frequency interval: 3–6 Hz was more significant. Low frequencies are more harmful to scoliosis patients.

To provide a more intuitive quantification of the peak changes at different frequencies, the maximum, minimum, and peak-bottom changes (maximum-minimum) of, T6 vertebral body axial displacement, T4–T5 disc bulge axial displacement, von-Mises stress in the matrix, and nucleus pulposus pressure at different frequencies were plotted (Table 5).

The magnitudes of the time-dynamic response at these five frequencies were ranked as 4 > 3 > 5 > 6 > 10 Hz. The closer the resonance frequency, the larger the peak. Compared to frequency of 6 Hz, the axial displacement of the vertebral body was 3.976 mm smaller, the axial displacement of the disc bulge was 4.86 mm smaller, the von Mises stress of the disc matrix was 60.52% lower, and the nucleus pulposus compressive

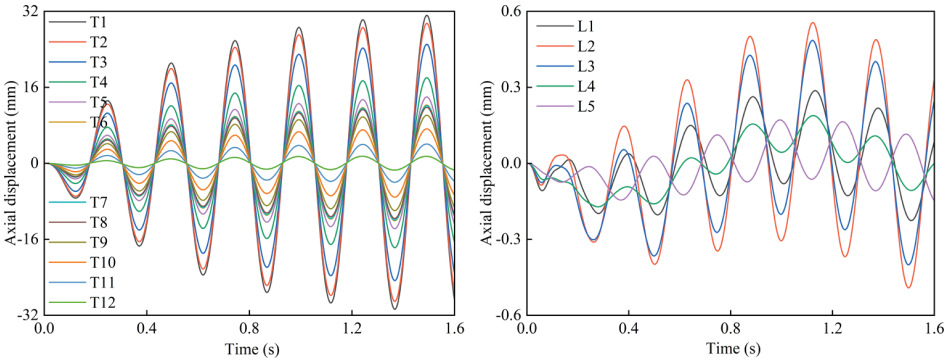


Fig. 7. Time-domain response of axial displacements of thoracic and lumbar vertebral bodies to sinusoidal axial loads at resonant frequencies

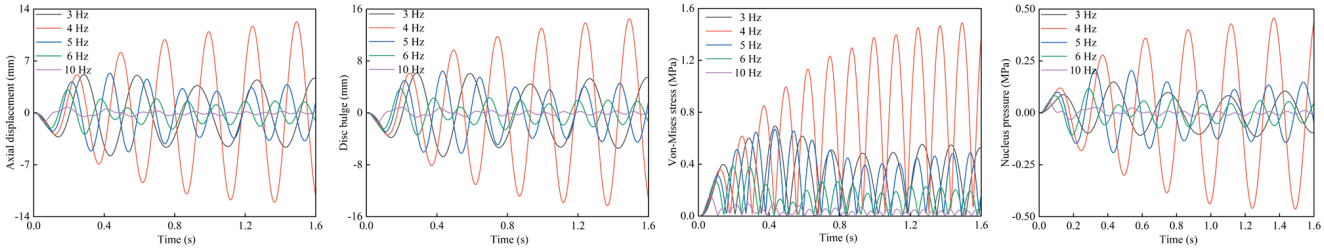


Fig. 8. Time-domain response at different frequencies

stress of the disc was 63.39% lower at 10 Hz compared with 6 Hz.

Table 5. Axial displacement and stress at different frequencies

| Frequency | | Axial displacement [mm] | Disc bulge [mm] | Stress in annulus [MPa] | Nucleus pressure [MPa] |
|---|---|---|---|---|---|
| | maximum | 5.162 | 6.145 | 0.695 | 0.149 |
| 3 Hz | minimum | –5.796 | –6.752 | 0.000 | –0.114 |
| | variation | 10.958 | 12.897 | 0.695 | 0.263 |
| | maximum | 12.275 | 14.514 | 1.489 | 0.456 |
| 4 Hz | minimum | –12.089 | –14.304 | 0.000 | –0.464 |
| | variation | 24.364 | 28.818 | 1.489 | 0.920 |
| | maximum | 5.362 | 6.437 | 0.669 | 0.207 |
| 5 Hz | minimum | –5.262 | –6.214 | 0.000 | –0.192 |
| | variation | 10.623 | 12.652 | 0.669 | 0.399 |
| | maximum | 3.079 | 3.702 | 0.385 | 0.117 |
| 6 Hz | minimum | –2.878 | –3.426 | 0.000 | –0.107 |
| | variation | 5.957 | 7.127 | 0.385 | 0.224 |
| | maximum | 0.771 | 0.852 | 0.152 | 0.050 |
| 10 Hz | minimum | –1.210 | –1.414 | 0.000 | –0.032 |
| | variation | 1.981 | 2.267 | 0.152 | 0.082 |

# 4. Discussion

Patients with severe AIS may even commit suicide in addition to suffering abnormalities in somatic function and severe psychological problems, especially in girls [2], and it is thus especially significant to investigate female patients with severe AIS. Because strain energy affects bone tissue regeneration and reconstruction [33], it is important to perform kinetic characterization of the spine preoperatively.

Although the thoracic spine has been studied by previous researchers, the depth of their analysis is insufficient. In 2010, Li et al. [23] established a three-dimensional finite element model of uni-thoracic curvature idiopathic scoliosis for the static analysis of axial loading, showing that uni-thoracic curvature scoliosis may lead to an uneven distribution of the structural stresses on the discs, articulating articular joints, and endplates of the entire spinal column. In 2020, Raja et al. [27] conducted a static mechanical analysis on the thoracolumbar segment of patients with scoliosis, performing a static analysis of its stress-strain and deformation, and found high stress concentrations on the vertebrae and intervertebral discs in the region affected by scoliosis, while in 2022, Li et al. [19] analyzed the displacement and stress of the AIS under the action of gravity, and found that there were localized stress concentrations on the concave side of the primary thoracic curve and the convex side of the pronated curve. These studies only performed static analyses without kinetic studies, and the technique of following loads to a finite element model of the thoracolumbosacral spine in severe AIS has not yet been applied to study the ki-

netics of severe Lenke1 patients. Thus, the present study focused on the kinetics of severe Lenke1 patients using the technique of following loads to analyze the kinetics.

The analysis showed that for Lenke1B+ patients, the frequency response fluctuation of the thoracic bending vertebrae was more drastic than that of the lumbar bending vertebrae, which was consistent with the results of the recent study conducted by Yufang et al. [39] in 2024. Through the results of steady-state and transient analysis based on modal analysis, it was found that patients were more sensitive to low-frequency vibration, which would produce the maximum stress-strain at resonance frequency, with the stresses showing a tendency toward local concentration which, combined with the consideration of realistic out-of-action loading environments, indicated that the low frequencies in the range of 3–4.5 Hz would be a serious danger to the health of the patients, consistent with the findings of Jia et al. [13], Zhang et al. [38] and Raja et al. [27]. In addition, this study compared the effects of cyclic loading at different frequencies on the thoracolumbosacral spine and found that frequencies near the resonance frequency were far more hazardous to patients than high frequencies, approximately 4.4–12.7 times more hazardous to patients.

Vertical resonance frequency increases the load transfer within the intervertebral disc, which may lead to disc herniation and degeneration [37]. Current biomechanical studies on the intervertebral discs have focused mainly on the lumbar spine [40]. In the present study, the intervertebral disc stress map of the thoracic and lumbar vertebrae under the resonance frequency is shown in Fig. 9. Under the resonance frequency, the maximum stress was focused locally on the left side of the intervertebral disc between vertebrae T4 and T5, with the maximum value of stress being 3.496 MPa, clearly indicating that this disc is the most susceptible to damage or degeneration. The safest and smallest stress is was seen at L5–S, with a stress of 0.007 MPa. It is thus obvious that the sacrum has the role of stabilizing the spinal column, and the intervertebral disc stress tends to be concentrated in the spinal deformity, and the closer the intervertebral disc is to the main curvature, the greater the stress concentration and the greater the stress.

Recent studies have indicated that excessive mechanical loading can cause osteoarthritis of the small joints [36]. Few finite element simulations have addressed the issue of the cartilage in the small joints, with the capsular ligaments either being ignored or replaced with springs in the model, resulting in limited information on the small joints [26]. In this study, the stress map of the small joints of the thoracolumbar vertebrae under resonance frequency is shown in Fig. 10. Under the resonance frequency, the maximum stress of the small joints was at the left small joint between the T7 and T8 vertebrae, with a maximum stress value of 19.97 MPa. The site of minimum stress was at the left small joint of L4–L5, with a value of 0.0531 MPa, while the maximum strain occured in the right small joints between the T6 and T7 vertebrae, with a maximum strain of 0.0531 MPa. The maximum strain was apparent at the right facet joint between the T6 and T7 vertebrae, with a deformation of 54.31 mm and minimum displacement of 0, i.e., it had no effect. It is thus apparent that the region of maximum stress does not necessarily correspond with the position of maximum strain, with the maximum stress located in the concave part of the main curvature and the maximum strain

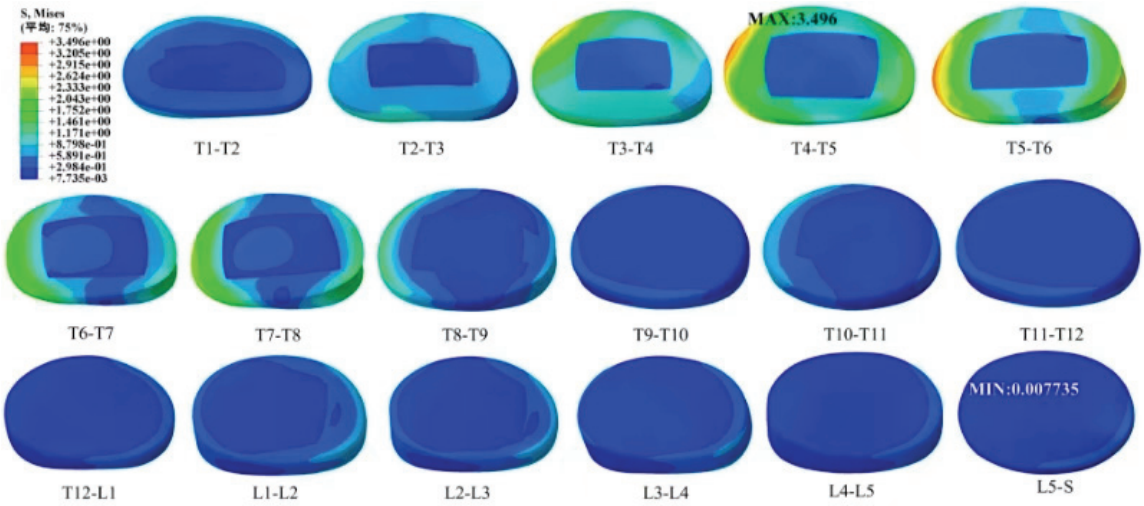


Fig. 9. Intervertebral disc stress clouds in the thoracolumbar spine at resonant frequencies

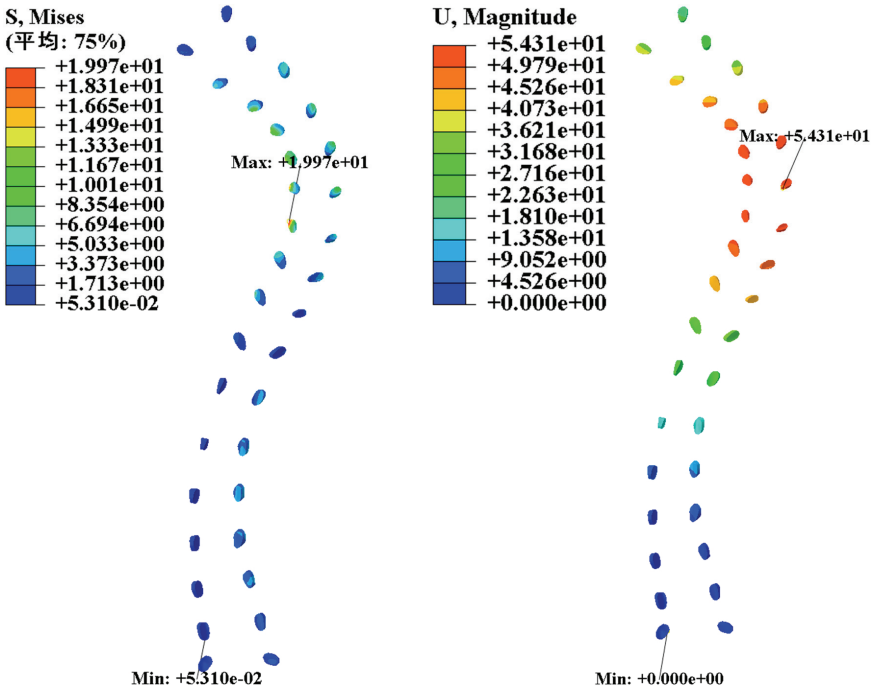


Fig. 10. Small joint stress clouds in the thoracolumbar spine at resonant frequencies

situated in the convex part of the main curvature. It is speculated that the concave part of the spine with the largest deformed segment in AIS is more prone to stress concentration, while the convex part of the spine is more prone to deformation.

The maximum value of the stress concentration in the intervertebral disc was smaller than the maximum value of the stress concentration in the small joints, indicating that while more researchers are focusing their attention on degenerative disc diseases, they should also pay attention to the prevention of small joint disorders, particulary to conditions such as subchondral sclerosis and hypertrophy of the small joints.

In this study, only the AIS finite element model of a female Lenke1B+ patient female was used for dynamic simulation calculations, while the FEM model was simplified for the human body, which is somewhat different from the actual situation.

The establishment of the small joints, joint capsule ligaments, and the use of compression follower preload simulation of muscle contraction and human gravity on the entire thoracolumbosacral spine physiological compression of the load enhanced the accuracy of the model. Furthermore, model validation included not only static validation, but also kinetic validation, suggesting the credibility of the simulation. The inclusion of the vertebral body of the spinal column, the intervertebral discs, and small joints provides a more comprehensive and in-depth analysis of the dynamics, and offers a theoretical basis for the design of clinical treatment programs for female Lenke1B+ AIS patients and assessment of their daily life risks.

## 5. Conclusions

Localized stress concentrations occur throughout the spine, with the spine showing greater fluctuations in the stress–strain curve the closer the spine is to the dynamic loading environment at the resonance frequency, indicating that patients should avoid exposure to similar resonance frequency environments.

Axial displacements and stress peaks in cyclic loading environments in the low-frequency range of 3–6 Hz were significant and these frequencies could thus potentially harm the health of patients, and patients are advised to stay away from environments in this frequency range.

The thoracic spine of patients with primary thoracic and secondary lumbar curvature is more sensitive to frequency response than the lumbar spine, and patients are thus reminded to protect the thoracic spine from collisions in their daily lives.

The concave areas of the largest deformed segments of the spine are more prone to load accumulation while the convex areas are more prone to large deformations; these areas tend to be the most susceptible to disc degeneration and small joint disease, and it is recommended for attention to be

paid to the examination of this area during clinical treatment.

## Acknowledgements

We thank the Sixth Affiliated Hospital of Xinjiang Medical University for providing patient CT data and medical guidance, the National Natural Science Foundation of China (Grant No. 32260235) for support, and the reviewers.

## References

[1] ALASSAF A., ALMOHIMEED I., ALGHANNAM M., ALOTAIBI S., ALHUSSAINI K., ALEID A., ALOLAYAN S., SIKKANDAR M.Y., ALHASHIM M.M., SHEIK S.B., SUDHARSAN N.M., *Time--dependent biomechanical evaluation for corrective planning of scoliosis using finite element analysis – A comprehensive approach*, Heliyon, 2024, 10 (5), e26946, DOI: 10.1016/j.heliyon.2024.e26946.

[2] AN J.K., BERMAN D., SCHULZ J., *Back pain in adolescent idiopathic scoliosis: A comprehensive review*, J. Child Orthop., 2023, 17 (2), 126–140, DOI: 10.1177/18632521221149058.

[3] DREISCHARF M., ZANDER T., BERGMANN G., ROHLMANN A., *A non-optimized follower load path may cause considerable intervertebral rotations*, J. Biomech., 2010, 43 (13), 2625–2628, DOI: 10.1016/j.jbiomech.2010.05.033.

[4] FAN W., *An in-limit elemental study of the dynamic properties of the human total lumbar spine in a vibration environment*, Northeastern University, 2017.

[5] FAN W., GUO L.X., *A comparison of the influence of three different lumbar interbody fusion approaches on stress in the pedicle screw fixation system: Finite element static and vibration analyses*, Int. J. Numer. Method. Biomed. Eng. 2019, 35 (3), e3162, DOI: 10.1002/cnm.3162.

[6] FAN W., GUO L.X., *Influence of different frequencies of axial cyclic loading on time-domain vibration response of the lumbar spine: A finite element study*, Comput. Biol. Med., 2017, 86, 75–81, DOI: 10.1016/j.compbiomed.2017.05.004.

[7] GOEL V.K., PARK H., KONG W.Z., *Investigation of vibration characteristics of the ligamentous lumbar spine using the finite element approach*, J. Biomech. Eng., 1994, 116 (4), 377–383, DOI: 10.1115/1.2895787.

[8] GUO L.X., FAN W., *Dynamic response of the lumbar spine to whole-body vibration under a compressive follower preload*, Spine, 2018, 43 (3), E143–E153, DOI: 10.1097/BRS.0000000000002247.

[9] GUO L.X., FAN W., *Impact of material properties of intervertebral disc on dynamic response of the human lumbar spine to vertical vibration: A finite element sensitivity study*, Med. Biol. Eng. Comput., 2019, 57 (1), 221–229, DOI: 10.1007/s11517-018-1873-5.

[10] GUO L.X., LI W.J., *Finite element modeling and static/dynamic validation of thoracolumbar-pelvic segment*, Comput. Methods Biomech. Biomed. Eng., 2020, 23 (2), 69–80, DOI: 10.1080/10255842.2019.1699543.

[11] GUO L.X., TEO E.C., LEE K.K., ZHANG Q.H., *Vibration characteristics of the human spine under axial cyclic loads: Effect of frequency and damping*, Spine, 2005, 30 (6), 631–637, DOI: 10.1097/01.brs.0000155409.11832.02.

[12] JIA S.W., LI Y., XIE J.D., TIAN T., ZHANG S.X., HAN L., *Differential response to vibration of three forms of scoliosis during axial cyclic loading: A finite element study*, BMC Musculoskelet Disord., 2019, 20 (1), 370, DOI: 10.1186/s12891-019-2728-4.

[13] JIA S.W., LIN L.Y., YANG H.F., XIE J.D., LIU Z.F., ZHANG T.Y., FAN J., HAN L., *Biodynamic responses of adolescent idiopathic scoliosis exposed to vibration*, Med. Biol. Eng. Comput., 2023, 61 (1), 271–284, DOI: 10.1007/s11517-022-02710-0.

[14] JIA S.W., ZHANG S.X., FAN S.C., LI Y., WU X.D., XIE J.D., HAN L., *Finite element analysis of lumbosacral vertebral structures in scoliosis and their deformation trends*, Journal of Medical Biomechanics, 2017, 32 (3), 235–241.

[15] KASRA M., SHIRAZI-ADL A., DROUIN G., *Dynamics of human lumbar intervertebral joints. Experimental and finite-element investigations*, Spine, 1992, 17 (1), 93–102, DOI: 10.1097/00007632-199201000-00014.

[16] KONG W.Z., GOEL V.K., *Ability of the finite element models to predict response of the human spine to sinusoidal vertical vibration*, Spine, 2003, 28 (17), 1961–1967, DOI: 10.1097/01.BRS.0000083236.33361.C5.

[17] KUZNIA A.L., HERNANDEZ A.K., LEE L.U., *Adolescent idiopathic scoliosis: Common questions and answers*, Am. Fam. Physician, 2020, 101 (1), 19–23.

[18] LAU K.K.L., KWAN K.Y.H., CHEUNG J.P.Y., CHOW W., LAW K.K.P., WONG A.Y.L., CHOW D.H.K., CHEUNG M.C.K., *Reliability of a three-dimensional spinal proprioception assessment for patients with adolescent idiopathic scoliosis*, Eur. Spine J., 2022, 31 (11), 3013–3019, DOI: 10.1007/s00586-022-07338-0.

[19] LI J.H., AN Z.C., WU J.G., GAO Y.C., LU S., HE D., ZHAO Y., *Construction of the adjusted scoliosis 3D finite element model and biomechanical analysis under gravity*, Orthop. Surg., 2023, 15 (2), 606–616, DOI: 10.1111/os.13572.

[20] LI P.J., FU R.C., YANG X.Z., WANG K., CHEN H.R., *Finite element method-based study for spinal vibration characteristics of the scoliosis and kyphosis lumbar spine to whole-body vibration under a compressive follower preload*, Comput. Methods Biomech. Biomed. Eng., 2024, DOI: 10.1080/10255842.2024.2333925.1-10.

[21] LI P.J., FU R.C., YANG X.Z., WANG K., *Dynamic response of idiopathic scoliosis to kyphosis*, Shanghai Jiao Tong University, 2023.

[22] LI Q.Y., KIM H.J., SON J., KANG K.T., CHANG B.S., LEE C.K., SEOK H.S., YEOM J.S., *Biomechanical analysis of lumbar decompression surgery in relation to degenerative changes in the lumbar spine – validated finite element analysis*, Comput. Biol. Med., 2017, 89, 512–519, DOI: 10.1016/j.compbiomed.2017.09.003.

[23] LI X.F., LIU Z.D., DAI L.Y., HU G.Y., WANG Z.Y., ZHONG G.B., ZANG W.P., *A study of the mechanism of the effect of axial loading on idiopathic scoliosis*, Chinese Journal of Pediatric Surgery, 2010, 31 (6), 435–439.

[24] LUO H.T., LIU G.M., FU J., YU C.S., *Vibration response analysis of the lumbar spine based on high-speed train crew*, 2017 IEEE 7th Annual International Conference on CYBER Technology in Automation, Control, and Intelligent Systems, 2017, DOI: 10.1109/cyber.2017.8446591. 220–224.

[25] MALMQVIST M., TROPP H., LYTH J., WIREHN A.B., CASTELEIN M.R., *Patients with idiopathic scoliosis run an increased risk of schizophrenia*, Spine Deform., 2019, 7 (2), 262–266, DOI: 10.1016/j.jspd.2018.07.003.

[26] PENG L., DUAN Z.L., LI Z.Y., LI J.H., LI Y.H., WANG S., LIU W.Q., *Current status and progress of research on finite*

*element modeling and validation of adolescent idiopathic scoliosis*, Tissue Engineering Research in China, 2023, 27 (27), 4393–4400.

[27] RAJA D., IYER S.R., PANDEY K., KRISHNAN A., PATIL S., *A biomechanical study of the scoliotic thoracolumbar spine*, IOP Conf. Ser. Mater Sci. Eng., 2020, 912, 022021, DOI: 10.1088/1757-899X/912/2/022021.

[28] RENNER S.M., NATARAJAN R.N., PATWARDHAN A.G., HAVEY R.M., VORONOV L.I., GUO B.Y., ANDERSSON G.B.J., AN H.S., *Novel model to analyze the effect of a large compressive follower pre-load on range of motions in a lumbar spine*, J. Biomech., 2007, 40 (6), 1326–1332, DOI: 10.1016/j.jbiomech.2006.05.019.

[29] SAMAAN M.C., MISSIUNA P., PETERSON D., THABANE L., *Understanding the role of the immune system in adolescent idiopathic scoliosis: Immunometabolic CONnections to Scoliosis (ICONS) study protocol*, BMJ Open, 2016, 6 (7), e011812, DOI: 10.1136/bmjopen-2016-011812.

[30] SMIT T.H., *On growth and scoliosis*, Eur. Spine J., 2024, 33 (6), 2439–2450, DOI: 10.1007/s00586-024-08276-9.

[31] STOKES I.A.F., GARDNER-MORSE M., *A database of lumbar spinal mechanical behavior for validation of spinal analytical models*, J. Biomech., 2016, 49 (5), 780–785, DOI: 10.1016/j.jbiomech.2016.01.035.

[32] WATKINS R., WATKINS R., WILLIAMS L., AHLBRAND S., GARCIA R., KARAMANIAN A., SHARP L., VO C., HEDMAN T., *Stability provided by the sternum and rib cage in the thoracic spine*, Spine, 2005, 30 (11), 1283–1286, DOI: 10.1097/01.brs.0000164257.69354.bb.

[33] WOLFF J., *Das gesetz der transformation der knochen*, Dtsch. Med. Wochenschr., 1892, 19 (47), 1222–1224.

[34] XIE J.D., ZHANG S.X., LI Y., JIA S.W., YANG H.F., CAO J., HAN L., *Dynamic properties of the adolescent idiopathic scoliotic spine*, Medical Biomechanics, 2018, 4 (33), 312–319.

[35] XU M., YANG J., LIEBERMAN I., HADDAS R., *Finite element method-based analysis for effect of vibration on healthy and scoliotic spines*, ASME 2016 International Design Engineering Technical Conferences and Computers and Information in Engineering Conference, 2016.

[36] YAHARA Y., SEKI S., MAKINO H., FUTAKAWA H., KAMEI K., KAWAGUCHI Y., *Asymmetric load transmission induces facet joint subchondral sclerosis and hypertrophy in patients with idiopathic adolescent scoliosis: Evaluation using finite element model and surgical specimen*, JBMR Plus, 2023, 7 (12), e10812, DOI: 10.1002/jbm4.10812.

[37] ZHANG C., GUO L.X., *Prediction of the biomechanical behaviour of the lumbar spine under multi-axis whole-body vibration using a whole-body finite element model*, Int. J. Numer. Method. Biomed. Eng., 2023, 39 (12), e3764, DOI: 10.1002/cnm.3764.

[38] ZHANG Q.L., CHON T., ZHANG Y., BAKER J.S., GU Y.D., *Finite element analysis of the lumbar spine in adolescent idiopathic scoliosis subjected to different loads*, Comput. Biol. Med., 2021, 136, 104745, DOI: 10.1016/j.compbiomed.2021.104745.

[39] ZHANG Y.F., LI S., LIU N., GUO H.W., QI X.H., MENG L., *Finite element modal analysis of the whole spine in adolescent idiopathic scoliosis*, Chinese Journal of Tissue Engineering Research, 2024, 28 (30), 4783–4787.

[40] ZHAO G., WANG H.W., WANG L.L., IBRAHIM Y., WAN Y., SUN J.Y., YUAN S.M., LIU X.Y., *The biomechanical effects of different bag-carrying styles on lumbar spine and paraspinal muscles: A combined musculoskeletal and finite element study*, Orthop. Surg., 2023, 15 (1), 315–327, DOI: 10.1111/os.13573.